UC Berkeley

Title

Printable, emissivity-adaptive and albedo-optimized covering for year-round energy saving

Permalink

https://escholarship.org/uc/item/54m861sw

Journal

Joule, 7(11)

ISSN

2542-4785

Authors

Li, Jiachen
Dong, Kaichen
Zhang, Tiancheng
et al.

Publication Date

2023-11-01

DOI

10.1016/j.joule.2023.09.011

Copyright Information

Peer reviewed

Printable, emissivity-adaptive and albedo-optimized covering for year-round energy savings

Jiachen Li[1,2,3,12], Kaichen Dong[1,4,5,6,12], Tiancheng Zhang[1,2,3], Derick Tseng[1], Cheng Fang[1], Ruihan Guo[1,2], Jingang Li[7], Yujie Xu[8], Chaochao Dun[9], Jeffrey J. Urban[9], Tianzhen Hong[8], Costas P. Grigoropoulos[7], Ali Javey[2,10], Jie Yao[1,2,3], Junqiao Wu[1,2,3,11]*

Affiliations:

[1]Department of Materials Science and Engineering, University of California, Berkeley, CA, 94720, USA.

[2]Materials Sciences Division, Lawrence Berkeley National Laboratory, Berkeley, CA, 94720, USA.

[3]Applied Science and Technology Graduate Group, University of California, Berkeley, CA, 94720, USA

[4] Tsinghua-Berkeley Shenzhen Institute, Tsinghua Shenzhen International Graduate School, Tsinghua University, Shenzhen, Guangdong, 518055, China

[5] Institute of Data and Information, Tsinghua Shenzhen International Graduate School, Tsinghua University, Shenzhen, Guangdong, 518055, China

[6] Center of Double Helix, Tsinghua Shenzhen International Graduate School, Tsinghua University, Shenzhen, Guangdong, 518055, China

[7]Department of Mechanical Engineering, University of California, Berkeley, CA, 94720, USA.

[8]Building Technology and Urban Systems Division, Lawrence Berkeley National Laboratory, Berkeley, CA, 94720, USA

[9]The Molecular Foundry, Lawrence Berkeley National Laboratory, Berkeley, CA, 94720, USA

[10]Department of Electrical Engineering and Computer Sciences, University of California, Berkeley, CA, 94720, USA.

[11] Lead contact

[12] These authors contributed equally

* Correspondence: wuj@berkeley.edu

Summary

Radiative cooling uses high-emissivity materials to passively cool the surface of outdoor objects such as building roofs on hot days. The issue of overcooling with this technology on cold days can be addressed by structures with thermal emissivity that is adaptive to temperature. Despite recent advances in temperature-adaptive structures, great challenges remain in their fabrication feasibility, and their unoptimized solar heating that may override the radiative cooling benefit. In

this work, we develop a printable, emissivity-adaptive and albedo-optimized covering (PEAC) based on recyclable materials with roll-to-roll fabrication. PEAC automatically switches its sky-window emissivity from 0.25 to 0.85 when the surface temperature exceeds a preset transition temperature, whereas delivering an albedo that is optimized for maximal year-round energy saving or thermal comfort in a given climate.

5

Introduction

The global demand for energy-efficient and sustainable temperature regulation solutions has been rapidly rising, driven by factors such as the energy crisis, climate change, and urbanization. As an attractive alternative or add-on to conventional heating, ventilation and air conditioning (HVAC) systems, radiative cooling has been extensively studied over the past few decades with wide application and commercialization[1-13]. It is based on the radiative emission of heat from terrestrial objects to outer space through the mid-IR atmospheric transparency window, which is known as the "sky window" ranging from 8 to 13 µm. Therefore, radiative cooling can efficiently reduce the temperature of, *e.g.*, buildings[1], vehicles[2,3], human bodies[4], and other objects without the need for external power sources or refrigerants. To radiate heat efficiently, passive radiative cooling materials are typically designed to have minimum absorptance in the solar wavelength range (0.3 to 2.5 µm) and maximum emissivity in the sky window. Such property has been realized in various materials such as wood[5], paints[6-8], fabrics[9,10], and dielectrics[11,12]. However, due to their static optical properties, most passive radiative cooling materials continue to radiate heat off objects even at ambient temperatures below the desired temperature, resulting in the unwanted overcooling of the objects in areas with large seasonal or daily temperature variations[13]. Since overcooling leads to discomfort as well as the need of additional energy for space heating, circumventing or alleviating the overcooling problem remains a significant challenge for the widespread implementation of radiative cooling technologies.

A range of temperature-adaptive technologies have been developed to mitigate the overcooling at low temperatures, including electrical dynamic glazing[14,15], mechanical-driven structures[16,17], and temperature-activated bimorph-based structures[18]. The requirements of external energy input or moving parts severely limit their energy efficiency and lifetime. Very recently, vanadium dioxide (VO$_2$) based Fabry-Perot (FP) resonators were realized to achieve self-switching in thermal radiation while avoiding those drawbacks[19-21]. However, the scalability and performance of these VO$_2$-based FP resonators are still restricted due to several factors. First, bounded by the FP resonance mechanism, the emissivity of these devices depends sensitively on the uniformity of the dielectric spacer thickness, leading to limited upgradability and increased difficulty for mass production. Second, the VO$_2$-based FP resonators are produced with expensive materials or fabrication methods which restrict their size and cost-effectiveness for scale applications. Last, the albedo of the structure is an equally important factor for the energy balance, which needs to be independently optimized for maximum energy saving in a given climate.

Here we present a printable, emissivity-adaptive, albedo-optimized covering (PEAC) as the solution (Table S1). This flexible covering is made through a roll-to-roll fabrication process using tungsten-doped VO$_2$ particles and inexpensive recyclable materials. As a temperature-adaptive radiative cooling structure, PEAC automatically switches the sky-window emissivity (ε_{sky}) from ~0.25 to ~0.85 when the surface temperature rises across a preset transition temperature (Figure 1A). The emissivity switching is enabled by in-plane inter-block photonic resonance, instead of cross-plane FP resonance, hence the performance of PEAC is independent of the thickness of the dielectric layer in the structure, enabling roll-to-roll fabrication (Figure 1B). Moreover, to maximize annual energy savings in different climates, PEAC can be customized with mid-IR transparent pigments to achieve optimal albedo as well as different visual colors (Figure 1C). Both rooftop and indoor temperature regulation of PEAC were

demonstrated in field experiments. Numerical simulations with climate database further demonstrate the energy-saving potential of PEAC across various climate zones in the US (Figure 1E).

5   **Results and Discussion**

PEAC design and fabrication

The PEAC functions as a radiative cooler only when the surface temperature (T_s) is high (Figure 1A). Such temperature-adaptive thermal emission is based on a unique photonic structure and the metal insulator transition (MIT) of vanadium dioxide (VO_2)[22-24]. As shown in Figure 2A and
10   Figure S5, the PEAC consists of a polyester (PET) substrate, an aluminum (Al) layer, a periodic array of tungsten-doped vanadium dioxide ($W_xV_{1-x}O_2$) blocks, and a polyethylene (PE) overlayer. The $W_xV_{1-x}O_2$ block array is carefully designed with guidance of numerical electromagnetic simulations while considering the fabrication feasibility and cost. The phase transition temperature (T_{MIT}) of VO_2 is approximately 68 °C, which can be reduced by doping with
15   tungsten to fit multiple applications (Figure S8). For instance, with 2% of W doping in VO_2, the corresponding T_{MIT} is about 20°C, suitable for household thermal regulation[25,26]. It is worth noting that PEAC is highly durable since $W_xV_{1-x}O_2$ is protected from air and water with the PE sealing (Figure S4, S9). Furthermore, the materials used, such as PE, PET, and Al, are all sustainable and recyclable[27], resulting a low lab cost of ~$1/sqft (Table S2).

20   We have developed a roll-to-roll printing process for mass production of PEAC, as illustrated in Figure 2A and Figure S1. Initially, the PE film is thermally micro-imprinted by a reusable metal template through a heated roller system. The reusable template is a metal sheet with a periodic array of micron-sized pillars constructed on the surface (Figure S2, S3). When the surface of the PE film is heated above 110°C, an array of pockets with identical dimensions are imprinted on
25   the surface of PE. Considering the heat capacity of the PE film, the temperature setpoint (T_{set}) of the rollers should increase with imprinting speed. We have achieved an imprinting speed that is approximately 100 meters per hour at $T_{set} = ¿$ 150°C. Subsequently, commercial $W_xV_{1-x}O_2$ nanoparticles are dispersed onto the patterned PE film surface by spraying a mixture of $W_xV_{1-x}O_2$ particles suspended in isopropyl alcohol. After mechanical pressing and surface cleaning, a PE
30   film embedded with a planar array of $W_xV_{1-x}O_2$ blocks is produced. Finally, the PEAC is formed by laminating the patterned side of the $PE/W_xV_{1-x}O_2$ film onto a pre-metallized PET substrate via running through another heated roller system. The entire fabrication process does not involve lithography or vacuum techniques, hence is scalable for mass production.

35   **Mechanism of PEAC**

The spectral thermal emissivity and solar absorptance of PEAC were accurately determined through spectroscopy measurements. The spectral reflectance of PEAC, $r(\lambda, T)$, was measured by a UV-vis-NIR spectrometer equipped with an integrating sphere, and a Fourier transform

infrared (FTIR) spectrometer. Since PEAC has zero transmittance to light, the spectral thermal emissivity $\varepsilon(\lambda, T)$ and spectral solar absorptance $a(\lambda, T)$ were calculated by $1-r(\lambda, T)$ in the mid-IR and UV-vis-NIR range, respectively. As depicted in Figure 2B, the thermal emissivity of PEAC exhibits a significant boost from low to high values when the temperature increases beyond the T_{MIT} of $W_xV_{1-x}O_2$, whereas the solar absorptance (A) of PEAC remains unchanged. To quantify the emissivity switching, ε_{sky} of PEAC is calculated from

$\varepsilon_{sky}(T) = \dfrac{\int \varepsilon(\lambda, T) B(\lambda, T) d\lambda}{\int B(\lambda, T) d\lambda}$, where the integration range is from 8 μm to 13 μm (sky-window),

and $B(\lambda, T)$ is the spectral intensity of blackbody radiation at temperature T. As shown in Figure 2C, ε_{sky} of PEAC switches from 0.25 to 0.85 over a typical roof temperature range.

The emissivity switching was investigated via finite element simulation. When the T is below T_{MIT}, the $W_xV_{1-x}O_2$ blocks are in the insulating state and thus largely transparent to IR radiation in the sky window[28]. As a result, most of the IR radiation is reflected by the Al layer underneath the $W_xV_{1-x}O_2$ blocks, resulting in a low absorptance/emissivity. However, at higher temperatures ($T > T_{MIT}$), $W_xV_{1-x}O_2$ switches to the metallic state with a large imaginary part of permittivity in the mid-IR. The mid-IR electromagnetic fields will be "funneled" into the gaps between neighboring $W_xV_{1-x}O_2$ blocks due to a large impedance mismatch between the $W_xV_{1-x}O_2$ blocks and the surrounding PE matrix. Hence, two neighboring $W_xV_{1-x}O_2$ blocks will form an optical antenna[29], and the electric field intensity at their surface is drastically enhanced, generating strong evanescent waves to be absorbed in the metallic $W_xV_{1-x}O_2$ blocks (Figure 3B). Consequently, the PEAC structure consisting of periodic $W_xV_{1-x}O_2$ blocks becomes an array of high-loss optical antennas, giving rise to high absorptance in the mid-IR (Figure 3C). According to Kirchhoff's law of radiation[30], the emissivity also switches from low to high values when the temperature rises across T_{MIT}. The high emissivity of PEAC at $T > T_{MIT}$ relies solely on the periodic array of the $W_xV_{1-x}O_2$ blocks and is independent of the thickness of the PE layer that merely acts as a protective encapsulation instead of a FP cavity spacer. This is further proved by both experiments and simulations, in which the general line-shape of the absorptance spectrum remains the same with the change in PE layer thickness, as shown in Figure S10, S11. Note that since the antenna absorptance does not depend on optical resonance at specific wavelengths, this switch in emissivity still exists even outside the sky window spectral range, benefiting applications in outer space[29] (Figure S6). Simulations prove the emissivity switching even at infinite PE thickness, hence the performance does not rely on a cross-plane FP resonance (Figure 3C). Such tolerance to layer thickness variation greatly eases the fabrication process, and opens the possibility of stacking or adding new functionality along the cross-plane direction, as shown below.

Pigment-aided albedo optimization

For real-world applications to fit different climates, albedo is an important factor since the heating from solar radiation, if not managed well, would easily offset the effect of radiative cooling (Figure 5D, Figure S19). With optimization of albedo, the year-round energy saving of PEAC in various climates can be greatly improved[31-34]. The albedo-optimization of PEAC is

enabled by adding a layer of pigments that are selectively absorptive in the solar range yet transparent in the mid-IR range. As shown in Figure 4A, the pigments can be dispersed onto the PEAC surface and then sealed with another layer of PE film. Due to the dominance of inter-block photonic resonance, the addition of pigments and the sealing PE layer affects only the position of the FP peaks, not the broadband trend in emissivity switching. This allows us to modify the solar reflectance (hence solar heating and visual color) without sacrificing the thermal emission switching in the sky window. By using BaF_2 (white), $ZnSe$ (yellow), Fe_2O_3 (red), Prussian Blue (blue) and their combinations, we are able to broadly tune the color and solar absorptance of PEAC (Figure 4B,1C). The colored PEACs also raise commercialization potential for aesthetic reasons.

The solar absorption spectra of the colored PEACs are shown in Figure 4C. The pigments tune the absorption of PEACs primarily in the visible range. Note that although different pigments have absorption peaks at different wavelengths, it is possible to have broadband absorption in the visible range with combinations of different pigments. The mid-IR spectral emissivity of the colored PEACs at both low and high temperatures was measured by FTIR spectroscopy (Figure S12), showing an evident insensitivity to the pigments added. ε_{sky} was calculated and shown in Figure 4D.

Thermal regulation and energy saving performance of PEAC

Outdoor temperature regulation experiments were conducted to test the performance of PEAC as a roof coating. A PEAC, a commercial dark roof coating product (BEHR #N520 Asphalt Gray), and a cool roof coating product (Henry Enviro-White Extreme Elastomeric Roof Coating) were used as roofs on three mock-up model houses (Figure S15). The model houses were 3D-printed with ABS filaments and were painted with white (walls) and dark (windows and doors) commercial paints[35]. To best simulate the heat exchange in real houses, the thermal resistance per area of the model house was carefully tuned to be close to that of real houses by adjusting the 3D-printing filling ratio and thickness of the walls and roofs[36,37]. The experiments were performed on cloudless summer days on a residential house roof in Berkeley, California (Figure 5A), and the real-time weather data were retrieved from a weather station near the experiment site.

The 24-hour record of the indoor temperature is shown in the middle panel of Figure 5B, whereas the left and right panels are zoom-in plots at cold night and hot noon, respectively. The temperature-time series show that during the night, the PEAC roof keeps the indoor temperature ~2°C higher than the other two roof materials, indicating that PEAC has switched to a low-emissivity, heat-retaining mode. In contrast, at noon under direct sunlight, PEAC performs as a cool roof delivering a cooler indoor temperature than that under the commercial dark roof, although with a slightly higher temperature than that under the commercial cool roof. It is known that the coefficient of performance (COP) of space heaters are generally much lower than those of air conditioners, and space heaters consume more energy annually[38,39]. Therefore, in this one-spot summer experiment, the better nighttime performance of PEAC over conventional cool roofs would indeed outweighs, in terms of overall energy saving, its worse cooling power at

daytime. From simulations considering typical house structure and COPs, the experimental temperature difference between PEAC and commercial white cool roof would lead to 78.61 kJ/m^2 energy saving over 24 hours (Details in Experimental Procedures). Other seasons have lower average temperatures compared to the summer, hence space heating takes larger portion in energy consumption, and PEAC would deliver better energy performance in other seasons than conventional cool roofs under the same HVAC system strategy. As a result, PEAC is expected to outperform the commercial cool roofs in terms of year-round energy saving due to its around-the-clock, all-season thermal regulation. Moreover, the roof temperature records (Figure S17) show that the temperature of PEAC remains above the dew point over the 24-hour period, while the other roofing materials are all cooled to the dew point temperature at night. Thus, PEAC is also effective in mitigating the well-known condensation problem of cool roofs[40,41]. In energy-poverty areas or scenarios where heating and air-conditioning are not available (*e.g.*, tents, or power outage times), PEAC would also reduce occupants' thermal discomfort because it cuts down the daily or seasonal temperature swing toward the pre-set, constant T_{MIT} during free-floating seasons, or in energy poverty areas (Figure S20).

We further analyzed the general performance of PEAC in household energy saving with numerical simulations. To estimate the energy saving of a roof material, we first calculated the hour-month map of equilibrium roof surface temperature T_s with TMY3 weather files included in the EnergyPlus climate database[42]. The result of using PEAC roof in Seattle, WA is shown in Figure 5C. We assumed that the building requires heating when T_s is lower than a heating setpoint $T_{h,set}$ (22°C) and needs cooling when T_s is higher than a cooling setpoint $T_{c,set}$ (24 °C)[19]. The heating/cooling efficiency of houses in different cities in the U.S. was extracted from past simulation results of cool roof energy savings to determine the total thermal regulation energy (E_{tr}) required to keep the building temperature between $T_{h,set}$ and $T_{c,set}$[19,43]. We define the energy saving ΔE_{tr} as the difference between E_{tr} of PEAC and E_{tr} of a representative cool roof material (fixed solar absorptance $A = 0.05$ and fixed ε_{sky}=0.95), where a positive value of ΔE_{tr} indicates that PEAC is more energy efficient. Therefore, ΔE_{tr} serves as a figure of merit of the energy-saving potential for a roof material. Figure 5D shows the dependence of E_{tr} on solar absorption for the colored PEACs, which proves again the importance of optimizing the albedo of a radiative cooling roof. As shown in Figure S19, the maximum total energy saving originates from the balance between solar heating and daytime radiative cooling with the optimal A that varies with different climate zones (Table S3). The simulated ΔE_{tr} for houses built before 1980 in cities representing the 15 US climate zones were illustrated in Figure 1E, showing that PEAC is more energy-efficient than conventional cool roofs in household temperature regulation in 12 of the 15 climate zones. For example, a PEAC roof with an area of 1700 sqft (158m^2) will save 12.63 GJ of energy each year for a typical single-family house built before 1980 in San Francisco, CA. This is equivalent to the elimination of 2,486 kg of carbon dioxide emission[44]. Further simulations predict that PEAC would outperform the conventional cool roof in all 15 climate zones if its albedo can be tuned to a wider range of values (Figure S18).

Conclusions

We have developed a printable, emissivity-adaptive, albedo-optimized covering (PEAC) that is roll-to-roll fabricated using recyclable materials. The roll-to-roll fabrication is enabled by the unique, cavity-free structure of PEAC, which eliminates the sensitive thickness dependence in previous temperature-adaptive radiative structures. Outdoor experiments and numerical simulations demonstrate PEAC's excellent temperature regulation and energy-saving potentials that are enabled by the automatic switching between the radiative-cooling mode and the heat-retaining mode. PEAC opens the possibility for large-scale applications of temperature-adaptive radiative coatings with aesthetic benefits. Buildings with PEAC applied to the envelope will be more thermal resilient during extreme hot or cold days coincident with power outages. Additionally, our simulation analysis on albedo-optimized temperature-adaptive radiative coolers can also serve as a guidance to future research on dynamic radiative coolers.

In the future, the emissivity switching would be made sharper if $W_xV_{1-x}O_2$ particle with higher quality could be used[45,46]. Machine-learning guided electromagnetic simulations on more complex photonic structures would further boost the performance of PEAC with reduced low-temperature emissivity and wider solar absorption range. Extension from roof application to wall application could be enabled by directional-emission photonic structures, which would bring further prospects in building energy saving[47].

PEAC can also be applied to objects beyond building roofs and walls, such as space objects, tents, and vehicles. Since PEAC switches emissivity in broadband thanks to the optical antenna design, it is ideal for outer space applications where the sky window is absent[48]. For heavy-duty applications such as tents and vehicle wraps, the mechanical strength of PEAC could be further enhanced by adding more supporting layers such as polyimide and Kevlar. The durability of PEAC can also be improved with the typical stitching method used in space multi-layer insulations[49,50]. As PEAC is free of a cavity layer and operates based only on in-plane photonic resonance, the pattern of PEAC can be imprinted onto a wide variety of polymer products including plastic shingles and containers. Moreover, by replacing the Al layer with transparent conducting oxides, an optically transparent PEAC could also be fabricated, which may find applications in window coating or greenhouse covering.

Experimental procedures

Resource availability

Lead Contact
Further information and requests for resources and materials should be directed to and will be
fulfilled by the lead contact, Junqiao Wu (wuj@berkeley.edu)

Materials Availability
This study did not generate new unique materials.

Data and materials availability
All data required to evaluate the conclusions in the manuscript are available in the main text or
the supplemental information.

Preparation of PEAC

Commercial PE food wrap (Saran Premium Wrap, S. C. Johnson & Son) was first imprinted by
passing through a laminator (ProLam Ultra-X Series Akiles Model X10) equipped with a nickel
(Ni) template which has micron-sized pillar patterns on it. The laminator consists of four pairs of
rollers, three of them are heated to a preset temperature and the last pair of rollers are at room
temperature. After the imprinting process, a mixture of isopropanol and sub-micron $W_xV_{1-x}O_2$
particles (Hongwu International Group Ltd., size further reduced by three hours of high-energy
ball milling) were spread onto the patterned PE film with an airbrush. The surface of the film was
cleaned by Texwipe, resulting in an array of $W_xV_{1-x}O_2$ blocks in the PE film. The PE film with
$W_xV_{1-x}O_2$ block array was laminated to an Al foil (Rhino Aluminum) or an Al/PET film
(McMaster-Carr) at the same temperature as that of the imprinting step to form the plain (non-
colored) PEAC. The colored PEAC was prepared with two more steps: infrared-transparent
pigments were first sprayed onto the non-colored PEAC surface. Subsequently, another layer of
PE film was laminated on top to seal the pigments (Figure S1). When PEAC is placed under a
light source, both specular reflection and diffraction grating colors are visible due to the
dominant reflection by the Al surface as well as scattering by the $W_xV_{1-x}O_2$ periodic structure.

The nickel template used in the imprinting process was fabricated as follows: The predesigned
inverse pattern, i.e. an array of holes, was created on a 675 μm thick Si wafer by standard
photolithography and ICP etching. A thin layer of Cr was subsequently sputtered onto the
patterned Si wafer as the seed layer. Then 20 μm-thick Ni was deposited onto the metallized Si
wafer by electroplating. After soaking in 20% KOH solution, the Ni layer will be separated from
the Si surface, forming a freestanding template (Figure S2). In order to integrate the Ni template
with the laminator, the Ni template was attached to a polyimide film (McMaster-Carr) and then
wrapped onto the rollers during mass production.

Spectrally resolved measurements

Thermal spectral reflectance at normal incidence, denoted as $r(\lambda, T)$, was characterized by a
Nicolet iS50 FTIR spectrometer and Nicolet Continuum microscope over the 8-14 μm
wavelength range. A blade aperture of 100 μm $\times$ 100 μm was used to select the area of interest.
All reflection spectra were normalized to the reflection spectrum of a 400 nm-thick aluminum

film. The temperature of the samples, ranging from 3 to 60 °C, was controlled by a dry ice cooled closed-loop thermal stage, connected to a Lakeshore 321 temperature controller. According to Kirchhoff's law of radiation, in a state of thermodynamic equilibrium, the spectral emissivity $\varepsilon(\lambda, T)$ is equal to the spectral absorptance $a(\lambda, T)$. Considering that the PEAC comprises a thick aluminum layer, its transmittance in both the solar and thermal infrared wavelength ranges was considered to be zero. Thus, its thermal spectral emissivity in this range was computed as $\varepsilon(\lambda, T) = a(\lambda, T) = 1 - r(\lambda, T)$. Near normal-hemispherical solar spectral reflectance, $r(\lambda)$, was measured from 300 nm to 2,500 nm with an Agilent Cary 5000 UV-vis-NIR spectrometer equipped with an Internal Diffuse Reflectance Accessory (DRA-2500), which captures both specular and diffuse reflections. Solar spectral absorptance was also computed as $a(\lambda) = 1 - r(\lambda)$ since the PEAC is essentially opaque to sunlight.

The solar absorptance A and sky-window thermal emissivity ε_{sky} can be calculated from the corresponding spectral data using the following formulas:

$$A = \left(\int_{0.3\,\mu m}^{2.5\,\mu m} I_s(\lambda) a(\lambda) d\lambda \right) / \left(\int_{0.3\,\mu m}^{2.5\,\mu m} I_s(\lambda) d\lambda \right) \tag{1}$$

$$\varepsilon_{sky}(T) = \left(\int_{8\,\mu m}^{14\,\mu m} B(\lambda) \varepsilon(\lambda, T) d\lambda \right) / \left(\int_{8\,\mu m}^{14\,\mu m} B(\lambda) d\lambda \right) \tag{2}$$

where $I_s(\lambda)$ is the spectral solar radiance, and B(λ) is the spectral intensity of blackbody emission.

Thermal infrared imaging and analysis

Thermal infrared images were acquired using a FLIR ONE infrared camera operating within the sky window wavelength range. To mitigate reflections from the camera and the surroundings, the default viewing angle was set as 20° instead of the normal incident direction. Additionally, a cryogen-cooled high emissivity plate was employed as the background.

During the capture of thermal infrared images, the camera measures the incident thermal infrared radiation and provides temperature readouts (T_{IR}) assuming a constant thermal emissivity (0.90) for the target. For a surface with a constant thermal emissivity, the T_{IR} vs. T_s relationship should exhibit approximately linear behavior. Consequently, the presence of a step feature in the T_{IR} vs. T_s curve signifies a transition in the emissivity of PEAC (Figure S8).

To justify that the emissivity-switching performance of PEAC is insensitive to angles, the angular dependence of the emissivity of PEAC at both high and low temperature (Figure S7) was experimentally measured. An IR camera was used to read T_{IR} of the same spot on PEAC from different angles, which directly related to the power of thermal radiation[51]. Note that the measurement starts from $\theta \approx 20\,°$ to avoid unwanted reflectance of IR power radiated from the IR camera itself. As shown in Figure S7B, the T_{IR} of PEAC remains almost unchanged at angles from $20\,°$ to $70\,°$ in both low-temperature and high-temperature states, indicating that the emissivity of PEAC is angle-insensitive, which is ideal for thermal regulation applications52

Durability test

To evaluate the durability of PEAC toward the day-to-night temperature cycles, we use a customized durability test system, which consists of an Arduino board (Mega 2560), a switch module (XY-GMOS), a DC power supply (Agilent 6645A) and a heating stage. The temperature of the heating stage is set to switch across the phase transition temperature (from 21°C to 70°C) of $W_xV_{1-x}O_2$ for a given number of cycles. A piece of PEAC sample was attached to the heating stage and the thermal emissivity was measured after 1, 10, 100 and 1000 cycles, respectively (Figure S9). We did not observe any delamination of the PEAC sample during this experiment, proving good mechanical stability during thermal cycling tests.

Simulation of device properties

The spectral absorptance of PEAC is numerically calculated using COMSOL Multiphysics, with all the geometric parameters matching the original design. The electromagnetic power loss density was calculated by:

$$p(r) = \frac{1}{2}\sigma E(r)^2 \tag{3}$$

Where σ is the electrical conductivity and $E(r)$ is the local electric field. For the antenna-only case simulation, the thickness of PE is set to be infinite to eliminate the FP resonance peaks. Note that the imaginary part of PE permittivity is slightly increased by fitting to better simulate the real case. Material properties are from published research articles[53-56]. We used an atomic force microscope (AFM) to measure the surface roughness of the $W_xV_{1-x}O_2$ side of a pressed $W_xV_{1-x}O_2$/PE film, which was peeled from an as-fabricated PEAC sample. The surface roughness R_a is only $11\,nm$, which is roughly 1/1000 of the working wavelength. With such low surface roughness, we can conclude that the particles are tightly compressed and the optical properties of $W_xV_{1-x}O_2$ blocks are close to a solid block at wavelengths around ~10 μm.

The design of the dimensions of the $W_xV_{1-x}O_2$ block array was optimized in two stages: First, the optimization was carried out using numerical electromagnetic simulation with COMSOL Multiphysics; Second, the design was further optimized with experimental tests. At the numerical electromagnetic simulation stage, the fabrication feasibility of the metal template was considered and the following dimensions of $W_xV_{1-x}O_2$ blocks were chosen as the starting point: height h=1.5 μm, width w=2.6 μm. Next, a parameter scan of h was performed with results shown in Figure S14A, showing that when h increases beyond 1.5 μm, the high-temperature state emissivity of PEAC decreases while the low-temperature state emissivity still increases. Thus, h =1.5 μm yields the highest emissivity tuning range. After the optimized value of h, a parameter scan of w was performed (Figure S14B), leading to the finding that the emissivity tuning range reaches maximum when w=3.6 μm. During the experimental tests of PEAC, w was slighted adjusted to w=3 μm due to the following four issues: (1) Although the simulated optimal w=3.6 μm promises the largest emissivity tuning range, it also leads to a high value of low-temperature emissivity (ε_{sky}=0.35), which works against the keeping-warm state at cold weather. (2) The holes on the imprinted polyethylene (PE) are too large when w=3.6 μm, causing structural instability during the $W_xV_{1-x}O_2$ particle deposition process as the walls between holes are too thin. (3) Larger w leads to higher solar absorptance as the $W_xV_{1-x}O_2$ particles cover too much

area on PEAC. (4) $W_xV_{1-x}O_2$ contributes to the majority of the cost, meaning that the cost of PEAC scales with w^2. The final nominal values of dimensions are shown in Figure S5.

To demonstrate the optical enhancement by the optical antenna formed by $W_xV_{1-x}O_2$ blocks, we also compared the high temperature spectral emissivity with other three other geometries of $W_xV_{1-x}O_2$ arrays: cylinder shape, pyramid shape and hemisphere shape. The cylinder shape of structure units is commonly used for emissivity regulation. The pyramid and the hemisphere shapes were achieved using KOH etching and isotropic etching, respectively, instead of ICP etching on Si surface during step 3 of template fabrication (Figure S2). The bottom width of all shapes is set to be identical as that of the $W_xV_{1-x}O_2$ blocks since the same lithography pattern is used. Figure S13 shows that the blocks array, which has parallel faces of neighboring blocks, has the best optical enhancement in terms of emissivity, proving the mechanism of antenna resonance and importance of the "optical funneling" effect.

Outdoor experiment setup

The model houses were 3D-printed with white ABS filament by a 3D-printer (Ultimaker 2+). With the reported thermal resistance of ABS 3D printing structure[36], we adjusted the thickness of walls and roofs, as well as the 3D printing filling ratio to achieve a thermal resistance per unit area similar to that of real houses[37]. To simulate the solar absorption characteristics of real houses, the walls of the model houses were painted white, while the windows were painted black. Two temperature sensors are embedded in each model house structure to measure the roof temperature and indoor temperature, respectively.

The model houses were placed on a roof of a residential house in Berkeley, CA. To mitigate the influence of uneven ground surfaces, a foam board was utilized. Throughout the experiment, temperature readings were recorded by a Raspberry Pi, while detailed weather data were obtained from a nearby weather station.

Thermal regulation simulation

We employed the energy-saving simulation method described in the published paper by Tang et al[19]. The stable surface temperature for a given material was calculated based on adiabatic approximation, assuming minimal heat transfer between the surface and the underlying structure. The climate parameters, such as air temperature (T_a), dew point temperature (T_d), wind speed (v), solar irradiance (I) and cloud coverage factor (CF) are obtained from TMY3 weather files available from the EnergyPlus database[42]. The sky-window emissivity of PEAC used in the simulation was calculated from the experimental spectra of FTIR measurements, and the solar absorptance was determined by the UV-vis-IR spectrometer measurements. With this setup, the all-year-around temperature maps (Figure 4C) of PEAC as well as all conventional materials with various static combinations of A and ε were calculated and compared.

We assumed that houses require heating when T_s falls below a heating setpoint $T_{h,set}$ (22 °C) and need cooling when T_s exceeds a cooling setpoint $T_{c,set}$ (24 °C). Subsequently, the energy consumption on space heating, ventilation, and air conditioning (HVAC) was calculated with the

temperature difference between T_s and setpoints. Regressed coefficients relating our surface temperature results to reported EnergyPlus simulation[43] specific to each climate zone and house type were reported in previous work[19]. Note that the building thermal inertia were considered in the EnergyPlus simulation reported by Rosado et al[43,57,58].

To demonstrate the energy efficiency advantage of PEAC over conventional cool-roof materials, the difference in source energy consumption for thermal regulation (ΔE_{tr}) between PEAC (with best performing A in the experimental range, Figure 4D) and a representative cool roof material ($A=\iota$ 0.05 and $\varepsilon_{sky}=\iota$ 0.95) was calculated in all 15 U.S. climate zones. The results in the energy saving calculations (Figure 1E, 5D, S17 and S18) are based on the pre-1980 single-family home, which is the dominant resident building type in the U.S.[59]. The heating, cooling, and total energy saving of PEAC over a representative cool roof are plotted in Figure S19. As the solar absorptance increases, heating energy saving rises, indicating that the building benefits more from passive solar heating in cold weather and requires less energy in space heating to maintain a desirable temperature. However, higher solar absorption also offsets the cooling energy saving of PEAC. As a result, an optimal solar absorptance that leads to maximum total energy saving exists and varies with different climate zones. The ΔE_{tr} results and corresponding optimal A for all types of single-family homes are presented in Table S2. The energy saving performance in hot climates are mainly limited by the lower limit of A. When A is sufficiently low, the difference in cooling energy saving between PEAC and the cool-roof material is as low as near-zero (Figure S19). Therefore, PEAC may outperform conventional radiative coolers in all the climate zones in the U.S. if an ideal solar absorptance range could be achieved (Figure S18).

The energy efficiency of PEAC over commercial cool roofs in the outdoor temperature regulation experiment has been demonstrated following the same method. The temperature difference between PEAC and commercial cool roof was extracted from the 24-hour experimental data, and the corresponding E_{tr} was calculated with reported regressed coefficients[19]. The resulting ΔE_{tr} between PEAC and the commercial cool roof material is 78.61 kJ/(m²·day). Note that this summer daily ΔE_{tr} is lower than 1/365 of numerically simulated year-round ΔE_{tr} in Berkeley, CA, predicting that the PEAC should be more energy efficient in other seasons.

To evaluate the temperature regulation (thermal comfort) advantage of PEAC in energy-poverty areas where heating and air conditioning are not used, a detailed numerical simulation was carried out with EnergyPlus. The simulation utilized a pre-1980 single-family house model, consisting of a living core zone, a garage, and an attic. The house model was generated from CBES[60] and San Francisco TMY3 weather data was used[42]. To simulate the condition in energy poverty area, the house is set to be un-conditioned. The emissivity of PEAC was set to be temperature-invariant outside of the atmospheric window, which leads to an underestimation of the thermal regulation performance of PEAC, as the emissivity switching also exists outside of the sky window (Figure S6). After the calculation of the hour-by-hour indoor temperature throughout a year, the temperature regulation ability, or comfort potential, of the roof material is characterized by the dimensionless figure of merit (FOM) defined as

$$FOM = \frac{T_{set,avg} \int dt}{\int |T(t) - T_{set,avg}| dt} \tag{4}$$

Here t is time and $T_{set,avg}$ is the average value of $T_{h,set}$ and $T_{c,set}$. Higher FOM indicates that the temperature $T(t)$ is more stable over time and temperature swing is narrower. We calculated the hourly temperature over a year for a house coated with non-colored PEAC and a house coated with a common commercial roof ($A = ¿ \, 0.9$ and $\varepsilon_{sky} = ¿ \, 0.9$), respectively. Figure S20 shows that the house under PEAC has higher FOM in all areas, which demonstrates PEAC's temperature regulation ability for the free-floating cases.

Author contributions

J.L., K.D. and J.W. conceived the general idea. J.L. and K.D. designed the material. J.L. and C.F. fabricated the material. J.L., K.D., T.Z., C.D., Jingang.L., C.P.G., J.J.U., and A.J. contributed to the spectral characterizations. J.L., K.D., T.Z., R.G., and J.W. performed the outdoor experiments. J.L., K.D., T.Z., Jingang.L., C.P.G., and J.Y. performed the numerical electromagnetic simulations. J.L., D.T., Y.X and T.H performed all other simulations. All authors discussed and analyzed the results. J.L., K.D., and J.W. wrote the manuscript with assistance from other authors. All authors reviewed and revised the manuscript.

Competing interests

A United States provisional patent application related to this work has been filed by J.W., J.L., and K.D.

References

1. Orel, B., Gunde, M. K., & Krainer, A. (1993). Radiative cooling efficiency of white pigmented paints. Solar energy, 50(6), 477-482. <https://doi.org/10.1016/0038-092X(93)90108-Z>.
2. Lv, Y., Huang, A., Yang, J., Xu, J., & Yang, R. (2021). Improving cabin thermal environment of parked vehicles under direct sunlight using a daytime radiative cooling cover. Applied Thermal Engineering, 190, 116776. <https://doi.org/10.1016/j.applthermaleng.2021.116776>.
3. Heo, S.Y., Lee, G. J., Kim, H., Kim, Y. J., Ishii, S., Kim, M. S., Seok, T. J., Lee, B. J., Lee, H., Song, Y. M. (2020). A Janus emitter for passive heat release from enclosures. Science advances, 6(36), eabb1906.<https://doi.org/10.1126/sciadv.abb1906>.
4. Xiao, R., Hou, C., Yang, W., Su, Y., Li, Y., Zhang, Q., Gao, P., Wang, H. (2019). Infrared-radiation-enhanced nanofiber membrane for sky radiative cooling of the human body. ACS applied materials & interfaces, 11(47), 44673-44681. <https://doi.org/10.1021/acsami.9b13933>.
5. Li, T., Zhai, Y., He, S., Gan, W., Wei, Z., Heidarinejad, M., Dalgo, D., Mi, R., Zhao, X., Song, J., et al. (2019). A radiative cooling structural material. Science, 364(6442), 760-763. <https://doi.org/10.1126/science.aau9101>.

6. Mandal, J., Fu, Y., Overvig, A. C., Jia, M., Sun, K., Shi, N. N., Zhou, H., Xiao, X., Yu, N., Yang, Y. (2018). Hierarchically porous polymer coatings for highly efficient passive daytime radiative cooling. Science, 362(6412), 315-319. <https://doi.org/10.1126/science.aat9513>.

7. Zhai, H., Fan, D., & Li, Q. (2022). Scalable and paint-format colored coatings for passive radiative cooling. Solar Energy Materials and Solar Cells, 245, 111853. <https://doi.org/10.1016/j.solmat.2022.111853>.

8. Li, X., Peoples, J., Huang, Z., Zhao, Z., Qiu, J., & Ruan, X. (2020). Full daytime sub-ambient radiative cooling in commercial-like paints with high figure of merit. Cell Reports Physical Science, 1(10), 100221. <https://doi.org/10.1016/j.xcrp.2020.100221>.

9. Zeng, S., Pian, S., Su, M., Wang, Z., Wu, M., Liu, X., Chen, M., Xiang, Y., Wu, J., Zhang, M. et al. (2021). Hierarchical-morphology metafabric for scalable passive daytime radiative cooling. Science, 373(6555), 692-696. <https://doi.org/10.1126/science.abi5484>.

10. Xie, B., Zhao, W., Luo, X., & Hu, R. (2023). Alignment engineering in thermal materials. Materials Science and Engineering: R: Reports, 154, 100738. <https://doi.org/10.1016/j.mser.2023.100738>.

11. Zhai, Y., Ma, Y., David, S. N., Zhao, D., Lou, R., Tan, G., Yang, R., Yin, X. (2017). Scalable-manufactured randomized glass-polymer hybrid metamaterial for daytime radiative cooling. Science, 355(6329), 1062-1066. <https://doi.org/10.1126/science.aai7899>.

12. Raman, A. P., Anoma, M. A., Zhu, L., Rephaeli, E., & Fan, S. (2014). Passive radiative cooling below ambient air temperature under direct sunlight. Nature, 515(7528), 540-544. < https://doi.org/10.1038/nature13883>.

13. Ulpiani, G., Ranzi, G., Shah, K. W., Feng, J., & Santamouris, M. (2020). On the energy modulation of daytime radiative coolers: A review on infrared emissivity dynamic switch against overcooling. Solar Energy, 209, 278-301. <https://doi.org/10.1016/j.solener.2020.08.077>.

14. Zhao, X., Aili, A., Zhao, D., Xu, D., Yin, X., & Yang, R. (2022). Dynamic glazing with switchable solar reflectance for radiative cooling and solar heating. Cell Reports Physical Science, 3(4), 100853. <https://doi.org/10.1016/j.xcrp.2022.100853>.

15. Rao, Y., Dai, J., Sui, C., Lai, Y.T., Li, Z., Fang, H., Li, X., Li, W. and Hsu, P.C. (2021). Ultra-wideband transparent conductive electrode for electrochromic synergistic solar and radiative heat management. *ACS Energy Letters*, *6*(11), 3906-3915. <https://doi.org/10.1021/acsenergylett.1c01486>.

16. Li, X., Sun, B., Sui, C., Nandi, A., Fang, H., Peng, Y., Tan, G., & Hsu, P. C. (2020). Integration of daytime radiative cooling and solar heating for year-round energy saving in buildings. Nature communications, 11(1), 6101. < https://doi.org/10.1038/s41467-020-19790-x>.

17. Xia, Z., Fang, Z., Zhang, Z., Shi, K., & Meng, Z. (2020). Easy way to achieve self-adaptive cooling of passive radiative materials. ACS applied materials & interfaces, 12(24), 27241-27248. <https://doi.org/10.1021/acsami.0c05803>.

18. Zhang, Q., Lv, Y., Wang, Y., Yu, S., Li, C., Ma, R., & Chen, Y. (2022). Temperature-dependent dual-mode thermal management device with net zero energy for year-round energy saving. Nature communications, 13(1), 4874. <https://doi.org/10.1038/s41467-022-32528-1>.

19. Tang, K., Dong, K., Li, J., Gordon, M. P., Reichertz, F. G., Kim, H., Rho, Y., Wang, Q., Lin, C-Y., Grigoropoloulos, C.P., et al. (2021). Temperature-adaptive radiative coating for all-season household thermal regulation. Science, 374(6574), 1504-1509. <https://doi.org/10.1126/science.abf7136>.

20. Wang, S., Jiang, T., Meng, Y., Yang, R., Tan, G., & Long, Y. (2021). Scalable thermochromic smart windows with passive radiative cooling regulation. Science, 374(6574), 1501-1504. <https://doi.org/10.1126/science.abg0291>.

21. Wang, Z., Kim, S. K., & Hu, R. (2022). Self-switchable radiative cooling. Matter, 5(3), 780-782. <https://doi.org/10.1016/j.matt.2022.01.018>

22. Morin, F. J. (1959). Oxides which show a metal-to-insulator transition at the Neel temperature. Physical review letters, 3(1), 34. <https://doi.org/10.1103/PhysRevLett.3.34>.

23. Wu, T. L., Whittaker, L., Banerjee, S., & Sambandamurthy, G. (2011). Temperature and voltage driven tunable metal-insulator transition in individual W x V 1− x O 2 nanowires. Physical Review B, 83(7), 073101. <https://doi.org/10.1103/PhysRevB.83.073101>.

24. Kim, C., Shin, J. S., & Ozaki, H. (2007). Effect of W doping in metal–insulator transition material VO2 by tunnelling spectroscopy. Journal of Physics: Condensed Matter, 19(9), 096007. <https://doi.org/10.1088/0953-8984/19/9/096007>.

25. Lee, S., Hippalgaonkar, K., Yang, F., Hong, J., Ko, C., Suh, J., Liu, K., Wang, K., Urban, J. J., Zhang, X., et al. (2017). Anomalously low electronic thermal conductivity in metallic vanadium dioxide. Science, 355(6323), 371-374. <https://doi.org/10.1126/science.aag0410>.

26. Batista, C., Ribeiro, R. M., & Teixeira, V. (2011). Synthesis and characterization of VO 2-based thermochromic thin films for energy-efficient windows. Nanoscale research letters, 6, 1-7. <https://doi.org/10.1186/1556-276X-6-301>.

27. Sardon, H., & Dove, A. P. (2018). Plastics recycling with a difference. Science, 360(6387), 380-381. <https://doi.org/10.1126/science.aat4997>.

28. Barker Jr, A. S., Verleur, H. W., & Guggenheim, H. J. (1966). Infrared optical properties of vanadium dioxide above and below the transition temperature. Physical Review Letters, 17(26), 1286. <https://doi.org/10.1103/PhysRevLett.17.1286>.

29. Dong, K., Deng, Y., Wang, X., Tom, K. B., You, Z., & Yao, J. (2018). Subwavelength light confinement and enhancement enabled by dissipative dielectric nanostructures. Optics Letters, 43(8), 1826-1829. < https://doi.org/10.1364/OL.43.001826>.

30. Agassi, J. (1967). The Kirchhoff-Planck Radiation Law: Considering Kirchhoff's law as it was initially meant may help us understand the rise of quantum theory. Science, 156(3771), 30-37. <www.jstor.org/stable/1720913>.

31. Xi, W., Liu, Y., Zhao, W., Hu, R., & Luo, X. (2021). Colored radiative cooling: How to balance color display and radiative cooling performance. International Journal of Thermal Sciences, 170, 107172.<https://doi.org/10.1016/j.ijthermalsci.2021.107172>.

32. Xie, B., Liu, Y., Xi, W., & Hu, R. (2023). Colored Radiative Cooling: Progress and Prospects. Materials Today Energy, 101302.<https://doi.org/10.1016/j.mtener.2023.101302>.

33. Lozano, L.M., Hong, S., Huang, Y., Zandavi, H., El Aoud, Y.A., Tsurimaki, Y., Zhou, J., Xu, Y., Osgood, R.M., Chen, G. et al. (2019)"Optical engineering of polymer materials and composites for simultaneous color and thermal management." Optical Materials Express **9**(5) 1990-2005. <https://doi.org/10.1364/OME.9.001990>.

34. Peng, Y., Fan, L., Jin, W., Ye, Y., Huang, Z., Zhai, S., Luo, X., Ma, Y., Tang, J., Zhou, J. et al (2022). Coloured low-emissivity films for building envelopes for year-round energy savings. Nature Sustainability, 5(4), 339-347. <https://doi.org/10.1038/s41893-021-00836-x>.

35. Wen, J., & Smith, T. F. (2002). Absorption of solar energy in a room. Solar energy, 72(4), 283-297. <https://doi.org/10.1016/S0038-092X(01)00107-4>.

36. Sonsalla, T., Moore, A. L., Meng, W. J., Radadia, A. D., & Weiss, L. (2018). 3-D printer settings effects on the thermal conductivity of acrylonitrile butadiene styrene (ABS). Polymer Testing, 70, 389-395. <https://doi.org/10.1016/j.polymertesting.2018.07.018>.

37. Treado, S. J. (1980). Thermal resistance measurements of a built-up roof system. Final report (No. PB-81-140063). National Engineering Lab.(NBS), Washington, DC (USA). <https://www.osti.gov/biblio/5759462>.

38. U.S. Energy Information Administration (2020). Annual Energy Review 2020 <https://www.eia.gov/totalenergy/data/annual/>.

39. U.S. Energy Information Administration (2015). 2015 Residential Energy Consumption Survey <https://www.eia.gov/consumption/residential/>.

40. Ahrab, M. A. M., & Akbari, H. (2013). Hygrothermal behaviour of flat cool and standard roofs on residential and commercial buildings in North America. Building and environment, 60, 1-11. <https://doi.org/10.1016/j.buildenv.2012.11.003>.

41. Bludau, C., Zirkelbach, D., & Künzel, H. M. (2008). Condensation problems in cool roofs.11th international conference on durability of building.

42. U.S. Department of Energy's Building Technologies Office (2022). EnergyPlus <https://energyplus.net/>.

43. Rosado, P. J., & Levinson, R. (2019). Potential benefits of cool walls on residential and commercial buildings across California and the United States: Conserving energy, saving money, and reducing emission of greenhouse gases and air pollutants. Energy and Buildings, 199, 588-607. <https://doi.org/10.1016/j.enbuild.2019.02.028>.

44. Greenhouse Gas Equivalencies Calculator, United States Environment Protection Agency <https://www.epa.gov/energy/greenhouse-gas-equivalencies-calculator>.

45. Chen, L., Huang, C., Xu, G., Miao, L., Shi, J., Zhou, J., & Xiao, X. (2012). Synthesis of thermochromic W-doped VO2 (M/R) nanopowders by a simple solution-based process. Journal of nanomaterials, 2012, 3-3. <http://dx.doi.org/10.1155/2012/491051>.

46. Liang, S., Shi, Q., Zhu, H., Peng, B., & Huang, W. (2016). One-step hydrothermal synthesis of W-doped VO2 (M) nanorods with a tunable phase-transition temperature for infrared smart windows. ACS omega, 1(6), 1139-1148. <https://doi.org/10.1021/acsomega.6b00221>.

47. Yu, N., Genevet, P., Kats, M. A., Aieta, F., Tetienne, J. P., Capasso, F., & Gaburro, Z. (2011). Light propagation with phase discontinuities: generalized laws of reflection and refraction. science, 334(6054), 333-337. < https://doi.org/10.1126/science.1210713>.

48. Dong, K., Tseng, D., Li, J., Warkander, S., Yao, J., & Wu, J. (2022). Reducing temperature swing of space objects with temperature-adaptive solar or radiative coating. Cell Reports Physical Science, 3(10), 101066. < https://doi.org/10.1016/j.xcrp.2022.101066>.

49. Finckenor, M. M., & Dooling, D. (1999). Multilayer insulation material guidelines (No. M-925). <https://ntrs.nasa.gov/citations/19990047691>.

50. Hatakenaka, R., Miyakita, T., Sugita, H., Saitoh, M., & Hirai, T. (2014). Development and testing of a zero stitch MLI blanket using plastic pins for space use. Cryogenics, 64, 121-134. <https://doi.org/10.1016/j.cryogenics.2014.02.018>.

51. Marinetti, S., & Cesaratto, P. G. (2012). Emissivity estimation for accurate quantitative thermography. NDT & E International, *51*, 127-134. <https://doi.org/10.1016/j.ndteint.2012.06.001 >.

52. Cho, J. W., Lee, Y. J., Kim, J. H., Hu, R., Lee, E., & Kim, S. K. (2023). Directional Radiative Cooling via Exceptional Epsilon-Based Microcavities. ACS nano.<https://doi.org/10.1021/acsnano.3c01184>.

53. Ordal, M. A., Bell, R. J., Alexander, R. W., Long, L. L., & Querry, M. R. (1985). Optical properties of fourteen metals in the infrared and far infrared: Al, Co, Cu, Au, Fe, Pb, Mo, Ni, Pd, Pt, Ag, Ti, V, and W. Applied optics, 24(24), 4493-4499. <https://doi.org/10.1364/AO.24.004493>.

54. Dong, K., Hong, S., Deng, Y., Ma, H., Li, J., Wang, X., Yeo, J., Wang, L., Lou, S., Tom, K.B., et al (2018). A Lithography-Free and Field-Programmable Photonic Metacanvas. Advanced Materials, 30(5), 1703878. <https://doi.org/10.1002/adma.201703878>.

55. Qazilbash, M. M., Brehm, M., Andreev, G. O., Frenzel, A., Ho, P. C., Chae, B. G., Kim, B.J., Yun, S.J., Kim, H.T., Balatsky, A.V et al. (2009). Infrared spectroscopy and nano-imaging of the insulator-to-metal transition in vanadium dioxide. Physical Review B, 79(7), 075107. <https://doi.org/10.1103/PhysRevB.79.075107>.

56. Querry, M. R. (1998). Optical constants of minerals and other materials from the millimeter to the ultraviolet. Chemical Research, Development & Engineering Center, US Army Armament Munitions Chemical Command. <https://apps.dtic.mil/sti/pdfs/ADA192210.pdf >.

57. California Energy Commission, *Building energy efficiency standards*. 1988, 2016 <http://www.energy.ca.gov/title24/>.

58. Huang, J., Hanford, J., & Yang, F. (1999). *Residential heating and cooling loads component analysis*. Building Technologies Department, Environmental Energy Technologies Division, Lawrence Berkeley National Laboratory, University of California. <https://p2infohouse.org/ref/36/35857.pdf>.

59. Energy Information Administration, Forms EIA-457A and EIA-457C of the 2015 Residential Energy Consumption Survey, Table HC2.1: Structural and Geographic Characteristics of U.S. Homes by Housing Unit Type, 2015. Available at: https://www.eia.gov/consumption/residential/data/2015/hc/php/hc2.1.php

60. Lawrence Berkeley National Laboratory, Commercial Building Energy Saver < https://cbes.lbl.gov/>.
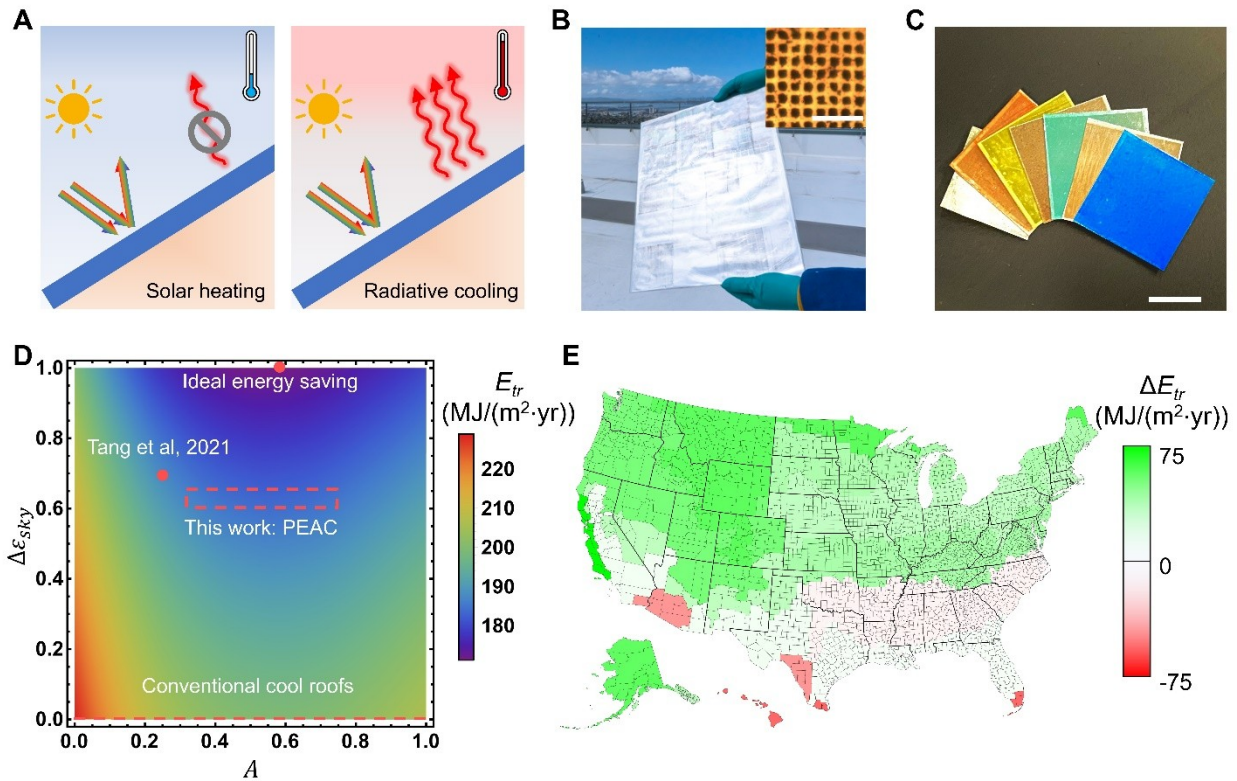
Main figure titles and legends

Figure 1. PEAC and its energy saving potential.
(A) schematic of household thermal regulation with a PEAC roof.
(B) A photo of a 30 cm by 40 cm roll-to-roll manufactured PEAC. Inset: an optical microscopic image of the PEAC structure. Scale bar: 20 μm.
(C) PEAC colorized with infrared transparent pigments. Scale bar: 1 cm.
(D) Simulated thermal regulation energy consumption (E_{tr}) to keep the indoor temperature of a single house between 22°C and 24°C in Seattle, WA. $\Delta\varepsilon_{sky}$ is the tuning range of emissivity (the emissivity difference between the high-temperature state and low-temperature state) of a covering, and A is solar absorptance. The ideal point and the work published in Tang *et al* [19] are also noted.
(E) Map of the energy saving (ΔE_{tr}) across the 15 climate zones in the U.S. by using PEAC in place of a conventional cool roof ($A = 0.05$ and $\varepsilon_{sky} = 0.95$).
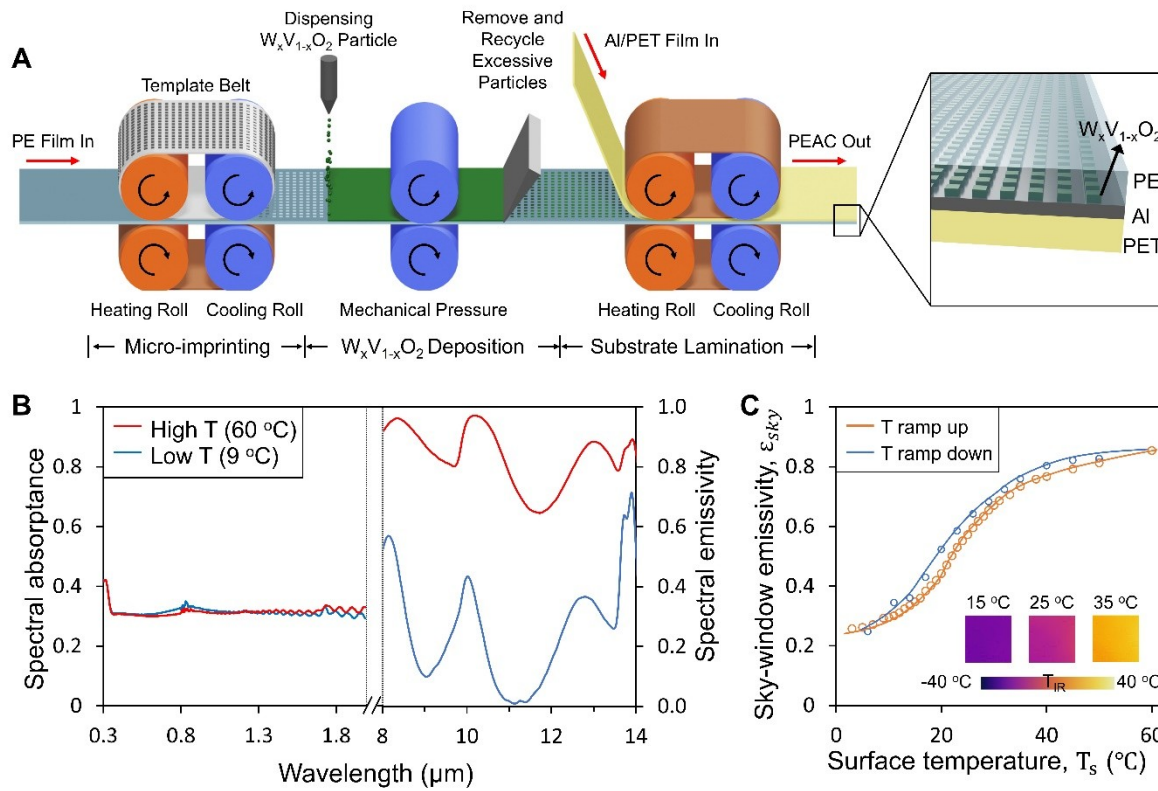
Figure 2. Fabrication process and spectral properties of PEAC.
(A) Roll-to-roll printing process to manufacture PEAC. Orange and blue rollers are at 110°C and room temperature, respectively.
(B) Spectrally resolved solar absorption and thermal emissivity of PEAC.
(C) Sky-window emissivity by integrating the measured spectral emissivity in the sky window. Inset: thermal images of PEAC taken at three different actual temperatures. T_{IR} is the temperature readout of the thermal camera.
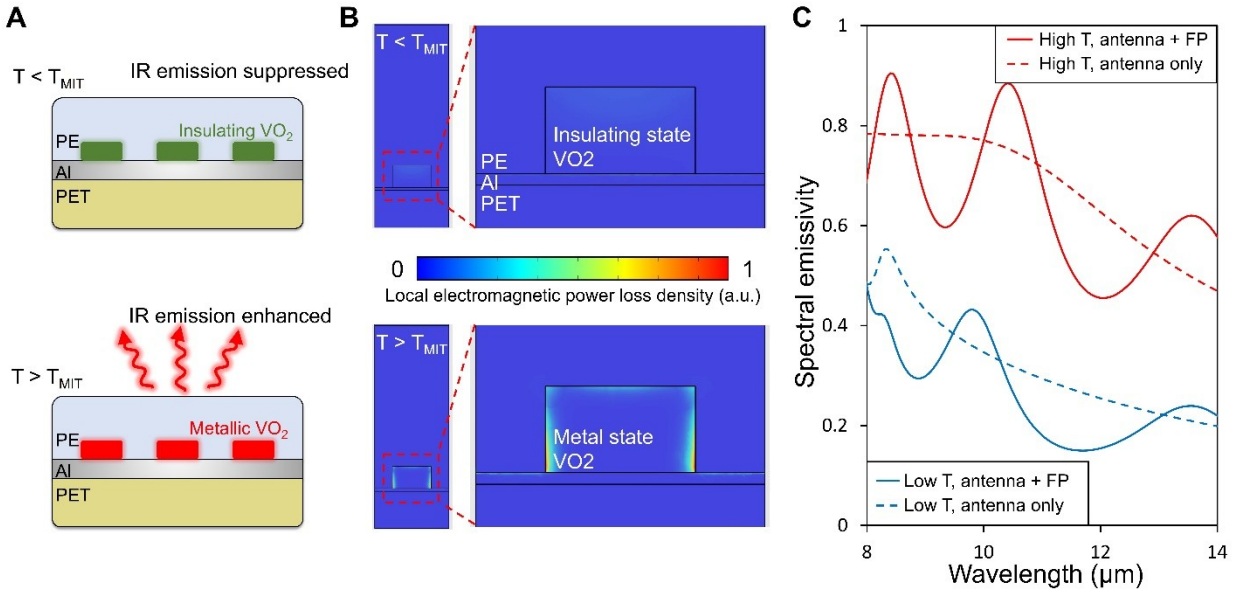
Figure 3. The working mechanism of PEAC.
(A) A schematic showing the in-plane photonic resonance mechanism of PEAC.
(B) Whole unit cell view (left) and zoom-in view (right) of mid-IR absorption profile in PEAC at
both low and high temperatures. The wavelength of incident light is 12 μm.
(C) Numerically calculated mid-IR absorption/emissivity, showing that the emissivity switch of
PEAC is dominated by the antenna mechanism. The dashed curves show the antenna-only
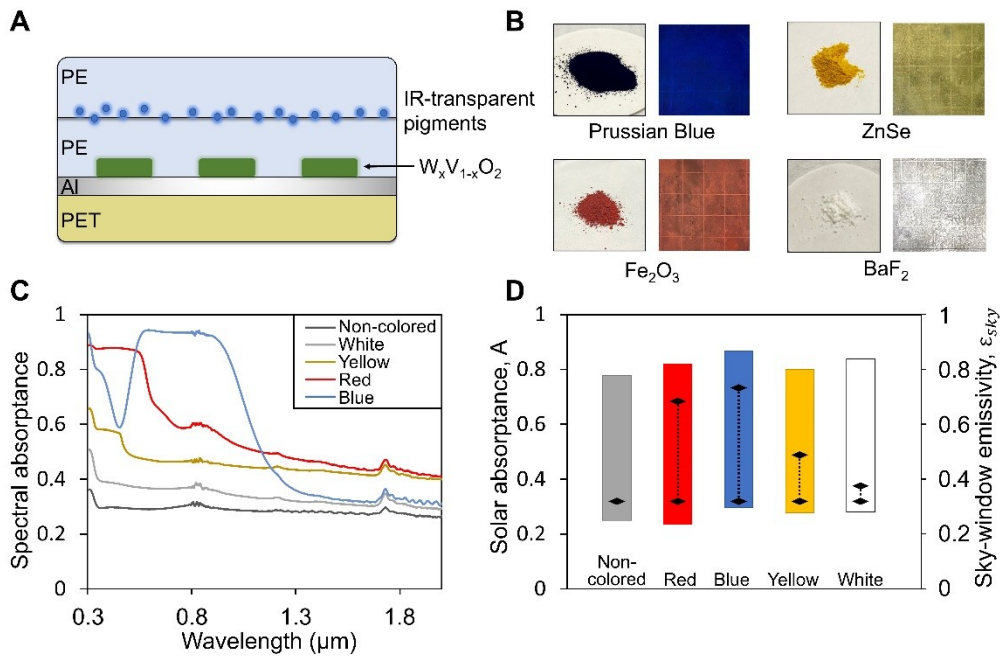scenario, in which the PE thickness is made infinite to eliminate the Fabry-Perot cavity.

Figure 4. Albedo optimization and colorization of PEAC.
(A) Cross-section schematic of colored PEAC.
(B) Photos of pigments and corresponding images of colored PEAC.
(C) Spectrally resolved solar absorptance of colored PEACs.
(D) Integral solar absorptance and sky-window emissivity of colored PEACs. The color bars show the range of temperature-adaptive sky-window emissivity (right axis) for the corresponding colored PEAC. The diamond markers show the solar absorptance (left axis) of each, and the dotted lines show the ranges of solar absorptance that can be tuned with the coverage of pigments.
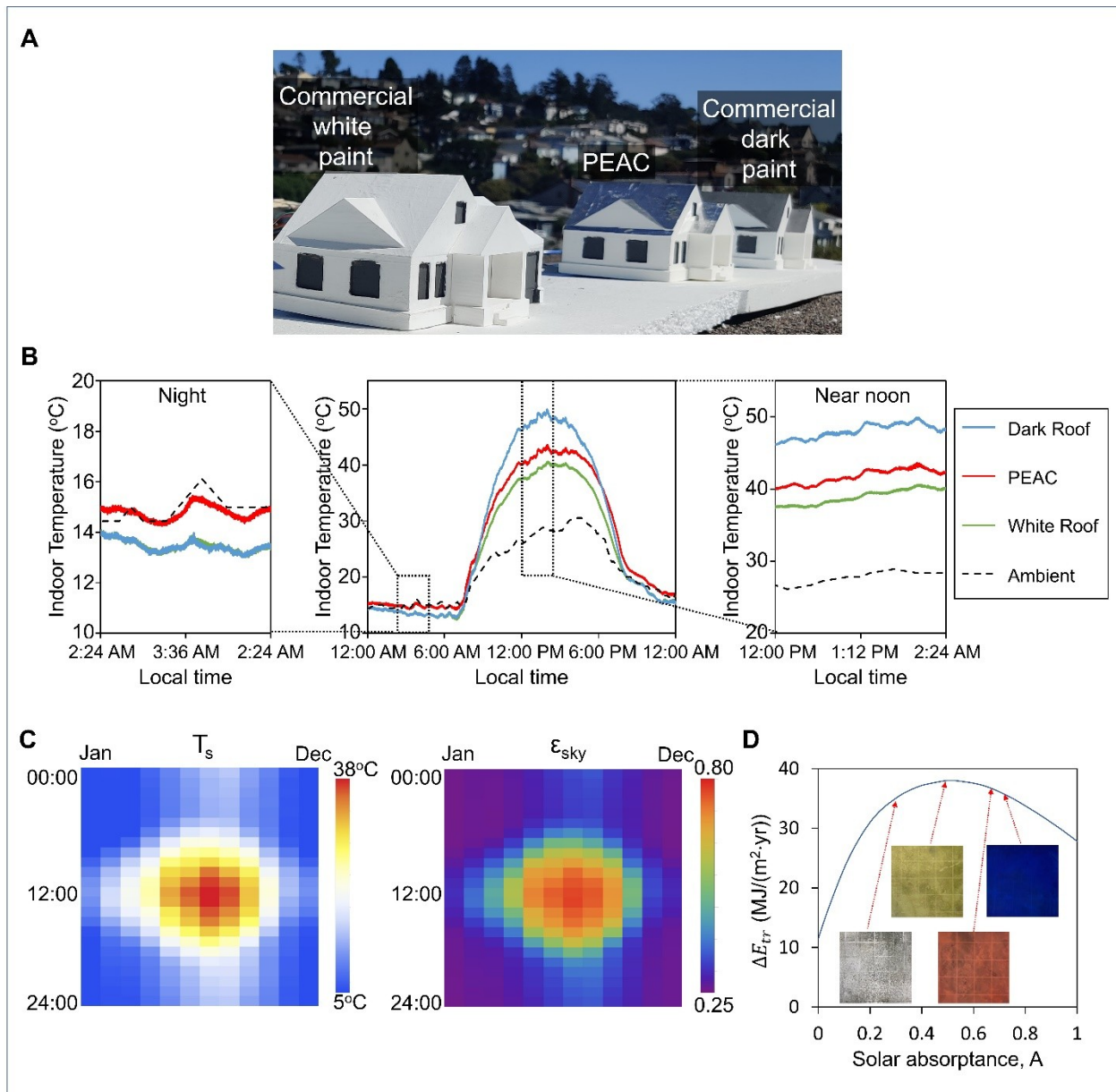
Figure 5. Outdoor performance of PEAC.
(A) Setup of the outdoor experiments.
(B) 24-hour recorded indoor temperature of the model houses covered with different roof materials. Left and right panels are scaled view of night and near noon, respectively. See also Figure S16
(C) Equilibrium surface temperature T_s and designed sky-window emissivity ε_{sky} of PEAC over the year.
(D) Extra energy saving (ΔE_{tr}) plot for a house equipped with colored PEACs in place of a cool roof material ($A = 0.05$ and $\varepsilon_{sky}=0.95$) in Seattle, WA.